Convective assembly of silica colloidal particles inside of photonic integrated chip based microfluidic systems for gas sensing applications

Valeriy Zaytsev,[*,§,a] **Aleksei Kuzin,**[*,§,a,b,c] **Krupamaya Panda,**[a] **Vasiliy Chernyshev,**[d] **Irina Florya,**[b] **Fedor S. Fedorov,**[a] **Vadim Kovalyuk,**[b,c] **Alexander Golikov,**[b,e] **Pavel P. An,**[e,h] **Boris N. Khlebstov,**[f,g] **Margarita Chetyrkina,**[a] **Albert G. Nasibulin,**[a] **Gregory Goltsman,**[c,h] **and Dmitry A. Gorin**[*,a]

[a] Center for Photonic Science and Engineering, Skolkovo Institute of Science and Technology, 30 Bld. 1 Bolshoy Boulevard, 121205, Russia. Address here.

[b] Laboratory of Photonic Gas Sensors, University of Science and Technology MISIS, 119049, Russia.

[c] National Research University Higher School of Economics, 101000, Russia.

[d] National Medical Research Center for Obstetrics, Gynecology and Perinatology named after Academician V.I. Kulakov, Ministry of Healthcare of the Russian Federation, 117198, Moscow, Russia.

[e] Department of Physics, Moscow State Pedagogical University, 119992, Russia.

[f] Institute of Biochemistry and Physiology of Plants and Microorganisms, Saratov, 410049, Russia.

[g] Saratov State University, Saratov, 410012, Russia.

[h] Quantum Photonic Integrated Circuits Group, Russian Quantum Center, Skolkovo, 143025, Russia.

[§] The authors contributed equally to this work

[*] Corresponding authors: valeriy.zaytsev@skoltech.ru; aleksei.kuzin@skoltech.ru; d.gorin@skoltech.ru

## S1. SURFACE COVERAGE ESTIMATIONS USING THE OTSU ALGORITHM

The surface coverage of the silica layers on Si_3N_4 the surface were processed using openCV Python package, version 3.3.9.7. Otsu thresholding[s1] with the minor code modifications. Feng *et al.* also implemented the OTSU algorithm to estimate the surface coverage of the monolayer films.[s2] The empty locations between the silica particles were designated as a background. As show in **Fig. S1**, following the conversion of an RGB SEM image to a gray scale image, a combination of binary conversion and Otsu's algorithm was applied.

Grayscale image   Binary image
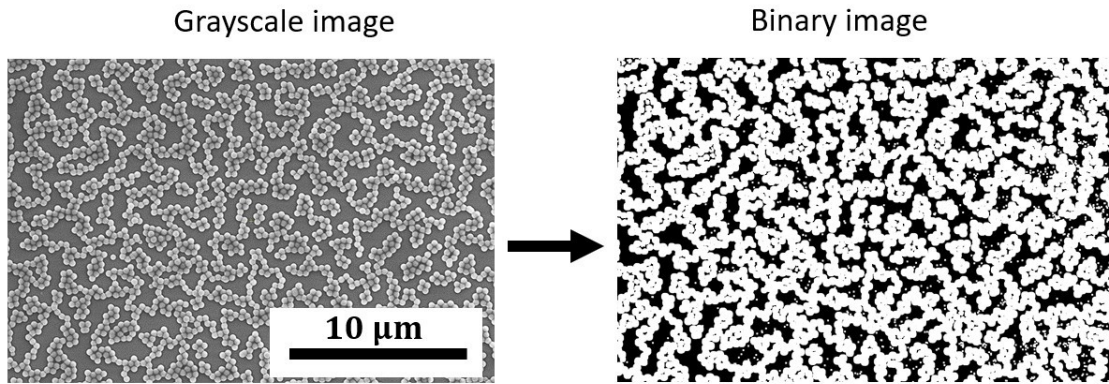
Fig. S1. Representation of processing a grayscale SEM image to a binary one by Otsu thresholding.

A grayscale image can be considered as a 2D matrix containing pixel values in the range of [0; 255], where 0 refers to black, and 255 refers to white. Then, a processed image undergoes several iterations of operations 'erode' and 'dilate'. The 'erode' operation helps in removing noises in the images, i.e., the other shades, and smooths out the pixels with most abundant pixel value. When 'erode' operation is applied, it removes the unnecessary white pixels from the background, while the use of 'dilate' function, which considers the background as noise, helps in eliminating the black pixels from the regions representing spherical particles.
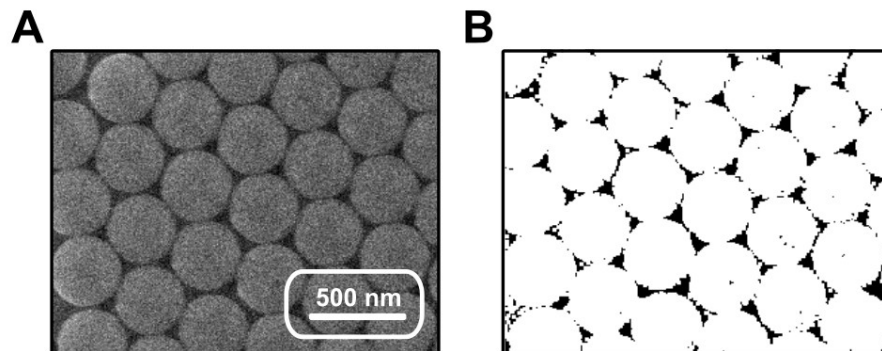
Fig. S2. Use of Otsu thresholding to a *hcp* silica monolayer.

We considered 5 to 10 images, where each image was obtained from a different number of 'dilate' iterations. After comparing the binary images with the original image, three images were selected. The final fill factor was the mean of fill factors calculated from these three images. Here, it is worth noting that the number of iterations for 'dilate' function can greatly influence on the fill factor. Thus, the decision if the binary image fits with the actual SEM image or not, solely depends upon the judgement of the user. This puts the factor of human error into the calculations. The use of this method for a binary image of a *hcp* monolayer of spherical silica particles (see **Fig. S2**) depicts a coefficient of surface coverage of 92 ± 3 % (n=3, P=0.95). This agrees well with the value of an ideal *hcp* monolayer, which is equal to $\frac{\pi}{2\sqrt{3}} \approx 90.7\ \%$. However, poor contrast between substrate and particle monolayers in SEM images will be a disadvantage of this method since it will be difficult to trace the boundaries between void and coated regions.

S2.   SUBSTRATE FABRICATION

We fabricated microfluidic channels by using soft lithography. The microfluidic chip contained polydimethylsiloxane (PDMS) channels with a square shaped cross-section 500 μm × 500 μm. A master-form of the microfluidic chip was obtained on acrylic plastic by using computer numerical control milling. To produce PDMS, a mixture of silicon elastomer and curing agent at a 10:1 ratio was prepared. To remove air-bubbles from PDMS prior to baking, the prepared mixture was placed inside the master-form structure and into a low vacuum chamber. The master-form containing PDMS was then baked at 60 $^{\circ}C$ for four hours. PDMS was then removed and washed with ethanol prior to its combination with the photonic chip.

For the fabrication of micro-ring resonators (MRRs), commercially available silicon nitride (Si_3N_4) substrates consisted of a 450 nm of low-pressure chemical vapour deposition Si_3N_4 on top of a silicon substrate with an initial 2.6 μm thick layer of SiO_2. For waveguide formation, electron beam lithography and then partial etching was done by using reactive ion etching (**Fig. S3a**). This resulted in 180 nm of partially etched rib waveguides (**Fig. S3b**) and focusing grating couplers (**Fig. S3c**). The fabricated photonic circuit had eight non-intersecting ring resonators with ring radius of 150 μm. The MRRs also had varying coupling gaps between bus and ring waveguides, i.e., 500 nm, 650 nm, 800 nm and 1000 nm. The MRRs in the opposite row had identical coupling gaps. The fabrication process was controlled with SEM and AFM techniques (**Fig. S3d**).
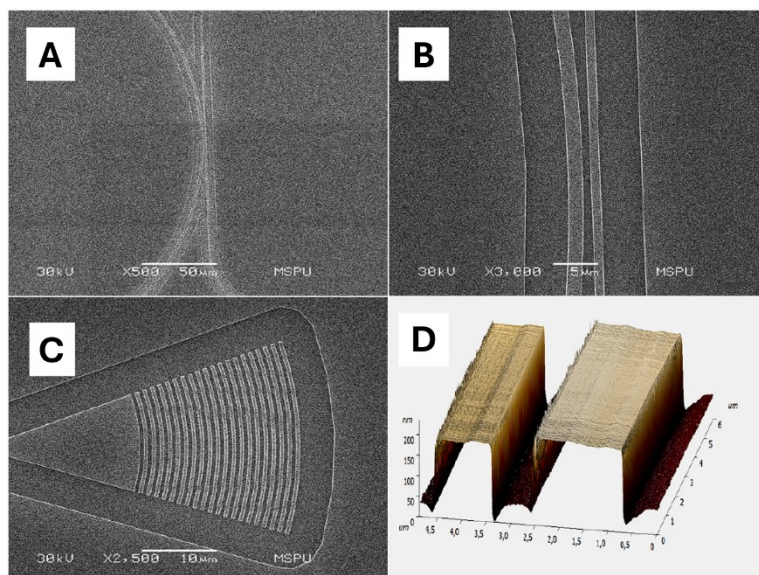

Fig. S3. Micro-ring resonator characterization. (a) SEM image of MRR. (b) SEM image of mode coupling gap region of MRR. (c) SEM image of focusing grating coupler. (d) AFM topography of gap region depicting the etching depth of less than 200 nm for photonic structures.
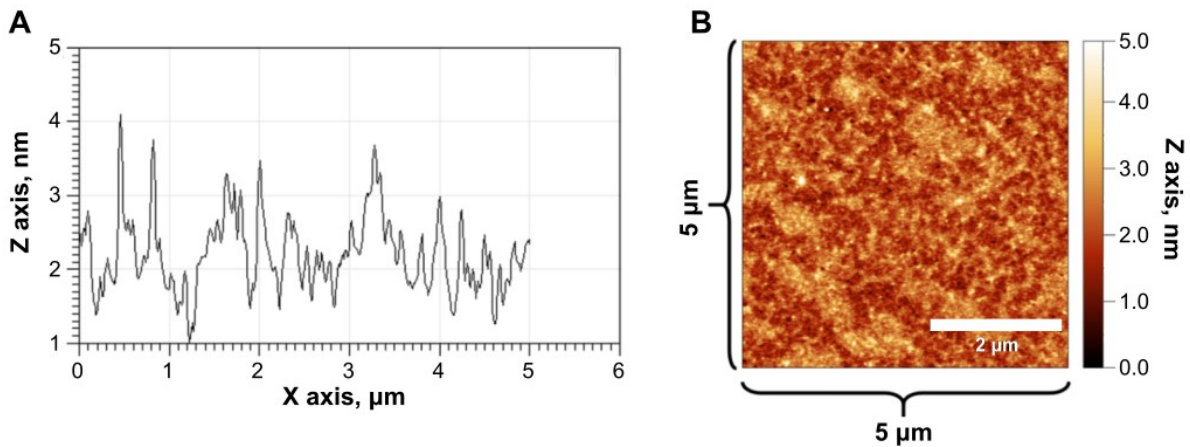
S3.   DIP COATING

Silicon nitride substrate cleaning protocol. Firstly, the contaminated surface was thoroughly washed with distilled water, followed by drying in the inert atmosphere. Then, to remove organic impurities from the surface, the following cleaning protocol was carried out: washing alternately with acetone (99.8%, EKOS-1) / propanol-2 (99.8%, EKOS-1) in an ultrasonic (US) bath for 7 minutes for each solvent, followed by washing with deionized water and drying. Afterwards, the surfaces of the substrates were cleaned in a "Piranha" solution (H_2SO_4: H_2O_2 (3: 1)) under US and a temperature of 50 °C for 15 minutes, then in a solution of NH_3 (25% solution) : H_2O: H_2O_2 (3: 1: 1) at the ultrasound and a temperature of 50°C within 15 minutes. The treated surface was washed in a stream of deionized water and dried in the inert atmosphere.

The preliminary cleaning of the surface using the RCA1 method[s3] was critical for forming a highly ordered silica monolayer. This can be explained by the more intense removal of organic and inorganic surface impurities by the alternating action of oxidizing agents, H_2SO_4 : H_2O_2 (3 : 1) and NH_3 (25% solution) : H_2O : H_2O_2 (3 : 1 : 1), respectively, and mechanical impurities by the action of ultrasound due to the cavitation effect.[s4]

76
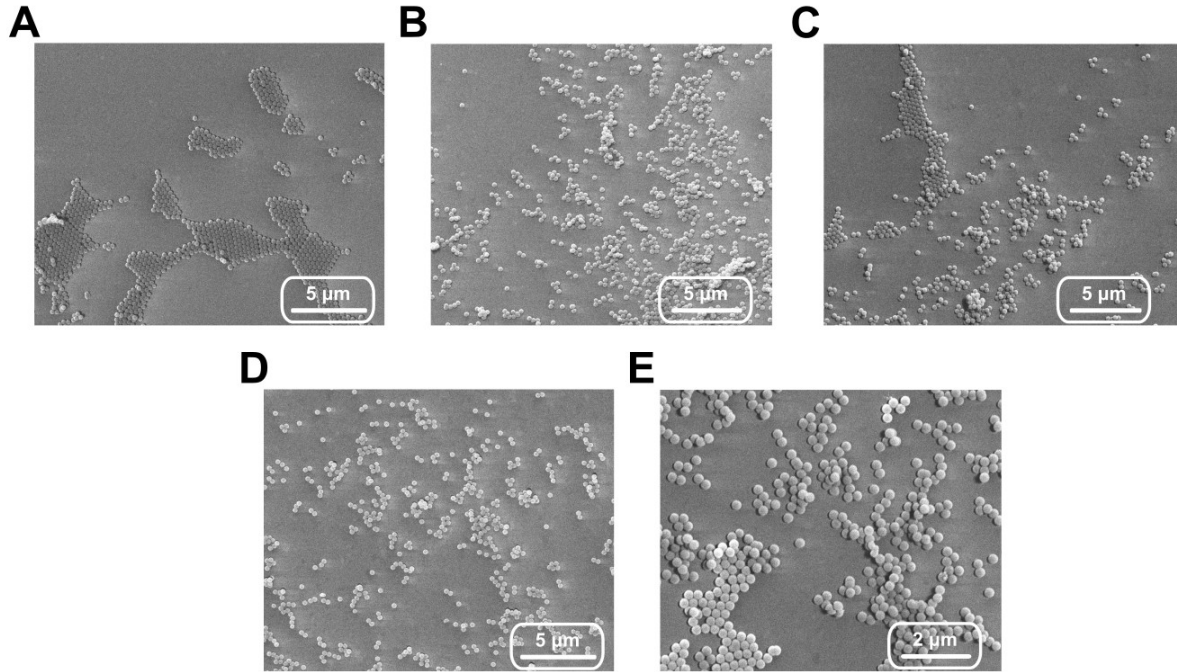
**Fig. S4. Influence of withdrawal speed on the SiO$_2$ layer deposition:** (**A**) $v_{withdrawal} = 0.6 \dfrac{mm}{min}$; (**B**) $v_{withdrawal} = 5 \dfrac{mm}{min}$; (**C**) $v_{withdrawal} = 14 \dfrac{mm}{min}$; (**D**) $v_{withdrawal} = 27 \dfrac{mm}{min}$; (**E**) $v_{withdrawal} = 41 \dfrac{mm}{min}$ (pristine Si$_3$N$_4$ substrate; $v_{dip} = 41 \dfrac{mm}{min}$; $t_{incubation} = 7\ min$).

80

Fig. S5. The estimation of a thickness (**A**) and topology (**B**) of the surface profile of PEI-modified surface in the microfludic channel.

82

83
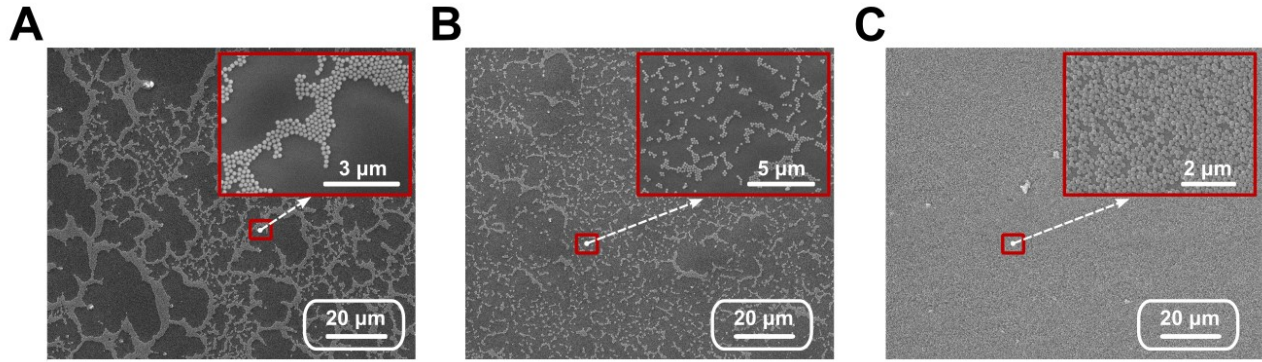
Fig. S6. Silica layer deposition by dip-coating: (A) pristine Si$_3$N$_4$ substrate; **(B)** PAH-modified Si$_3$N$_4$ substrate; **(C)** PEI-modified Si$_3$N$_4$

substrate ($v_{dip} = 41\dfrac{mm}{min}$; $t_{incubation} = 7\ min$; $v_{withdrawal} = 1\dfrac{mm}{min}$).

Landau-Levich equation:

$$h = c \cdot \frac{(\eta \cdot v)^{2/3}}{\gamma_{lv}^{1/6} \cdot (\rho \cdot g)^{1/2}},$$

(1)

where h - the film thickness; c – non-dimensional empirical coefficient; η – viscosity of medium; v – withdrawal rate of a Si$_3$N$_4$

substrate; $\gamma_{a/l}$ – surface tension of air/liquid interface; ρ – SiO$_2$ density; g – gravity.

S4. CONVECTIVE ASSEMBLY IN MICROFLUIDICS

SEM images of the particles assembled inside a microfluidic channel of width 500 μm and height 500 μm are presented in **Fig. S7**. The Si$_3$N$_4$ surfaces were pristine and cleaned using the substrate cleaning protocol. Here, we observed that the particles organized separated island aggregates due to capillary forces and inert features of the silicon nitride surface. Additionally, **Fig. S10** demonstrates aggregated non-homogeneous multilayer structures at the channel borders due to movement of the meniscus with a flow rate slower than in the central part of the channel.

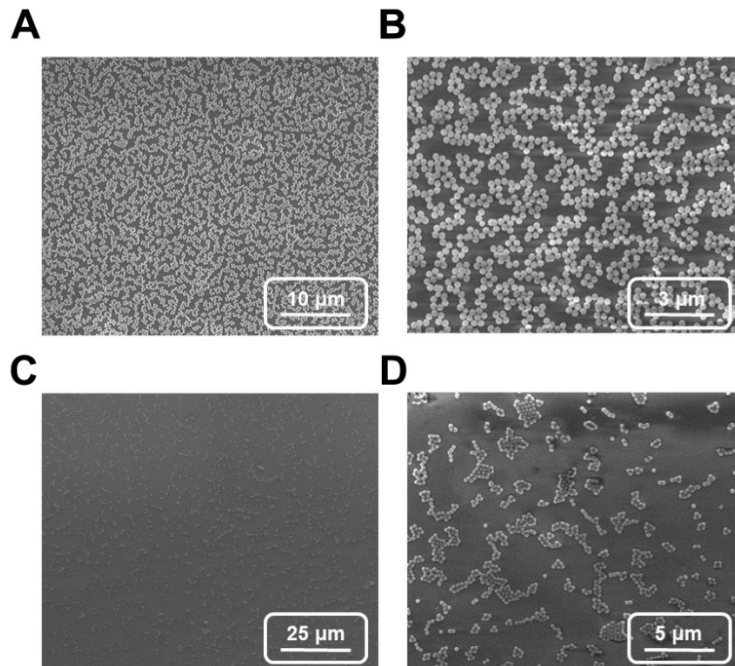97
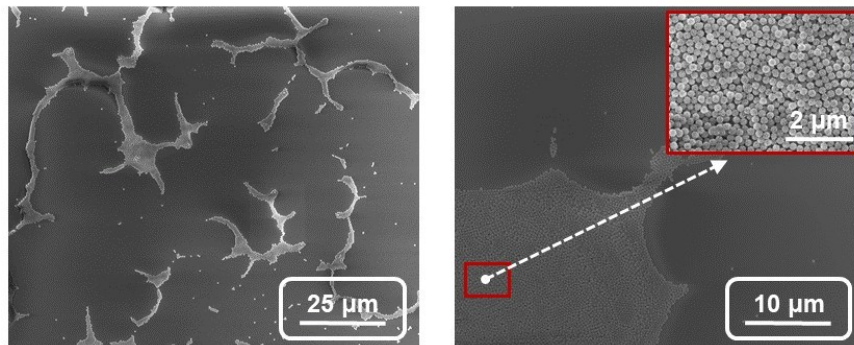
Fig. S7. Microfluidic deposition of silica layers on the pristine Si$_3$N$_4$ surface. (

$v_{filling} = 5\dfrac{\mu L}{min}$; $v_{outflow} = 15\dfrac{\mu L}{h}$; $t_{stabilization} \approx 2\ min$; the channel parameters: 500 μm × 500 μm)

100   **S5.   SILICA COATINGS ON PEI and PSS MODIFIED SILICOM NITRIDE SURFACES**

101

102

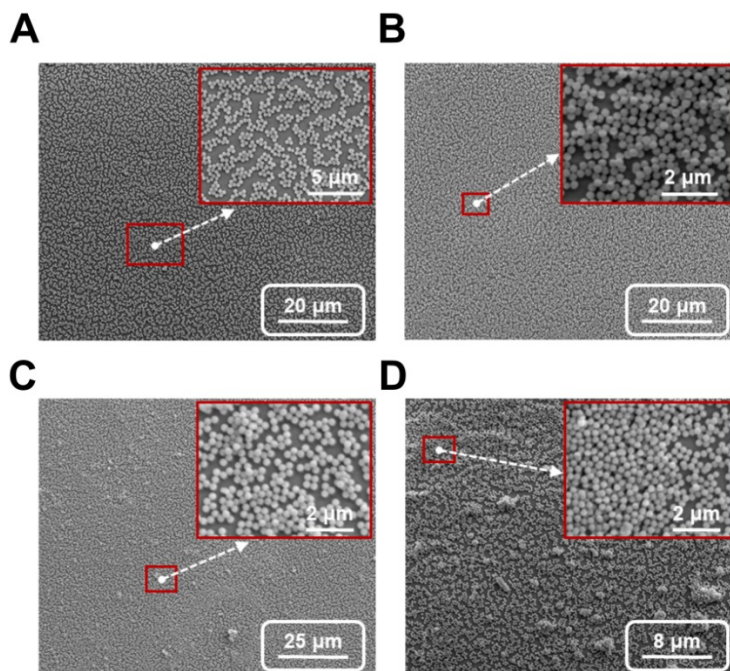103   **Fig. S8. Silica deposition on the polyelectrolyte modified Si$_3$N$_4$ surface by microfluidic deposition: (A, B)** PEI-modified channel;

$$v_{filling} = 5\frac{\mu L}{min}; v_{outflow} = 50\frac{\mu L}{h}; t_{stabilization} \approx 2\ min;$$

104   **(C, D)** PSS-modified channel (the channel parameters: 500 μm ×
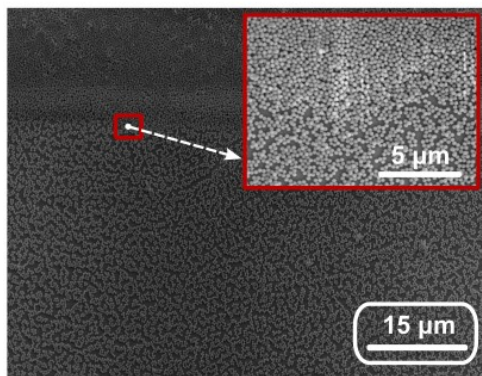105   500 μm).

106

107   **Fig. S9. Silica deposition on the PEI-modified Si₃N₄ surface by microfluidics under different suspension flow rates: (A)**

108 $v_{outflow} = 10\frac{\mu L}{h}$;   **(B)** $v_{outflow} = 25\frac{\mu L}{h}$;   **(C)** $v_{outflow} = 50\frac{\mu L}{h}$;   **(D)** $v_{outflow} = 100\frac{\mu L}{h}$ (

109 $v_{filling} = 5\frac{\mu L}{min}$; $t_{stabilization} \approx 2\ min$;   the channel parameters: 500 μm × 500 μm).

110

**111**   **Fig. S10. Microfluidic deposition of silica layers on the PEI-modified Si₃N₄ surface.** (

112 $v_{filling} = 5\frac{\mu L}{min}$; $v_{outflow} = 50\frac{\mu L}{h}$; $t_{stabilization} \approx 2\ min$;   the channel parameters: 500 μm × 500 μm)

113   **S6**   **INFLUENCE OF THE FORMED SILICA MICROSPHERE LAYERS ON THE SENSOR PERFORMANCE**

114   Synthesis and characterization of spherical submicron silica particles (SiO_2 SMPs) was demonstrated in our previously published

115   work.[s5] A comparison of particles' average diameters was provided *via* transmission electron microscopy (TEM) and dynamic light

116   scattering (DLS) methods (299 ± 3 nm). Particle average diameters were not invariably similar due to the presence of aggregates,

117   the number of which depends on the holding time of SiO_2 SMP suspensions in an ultrasonic bath. The value of ζ-potential is - 56

118   ± 2 mV, which indicates high colloidal stability of the synthesized silica particles.

119   The uniformity in diameter and sphericity of the silica microspheres directly affects the average Q factor of the micro-ring

120   resonators. In the case of slightly changed diameters of SiO_2 SMPs (299 ± 3 nm), optical losses at the central wavelength equal

121   to 1550 nm will be negligible. **Fig. S11** demonstrates the results of the simulation for estimation of the influence of the SiO_2 SMPs

122   on the Q factor performed in COMSOL Multiphysics. A 2D model of the waveguide cross-section was used to calculate the effective

123   refractive index (n_{eff}) and attenuation constant for fundamental TE and TM modes, characterized the interaction of evanescent

124   optical mode with the SiO_2 SMPs. A low optical power loss signifies a high Q factor and sharper resonance peaks, which translates

125   to improving the limit of detection (LoD) caused by gas adsorption. Non-uniform particles would introduce variability in the

126   resonance conditions, broadening the resonance peaks and reducing the LoD.
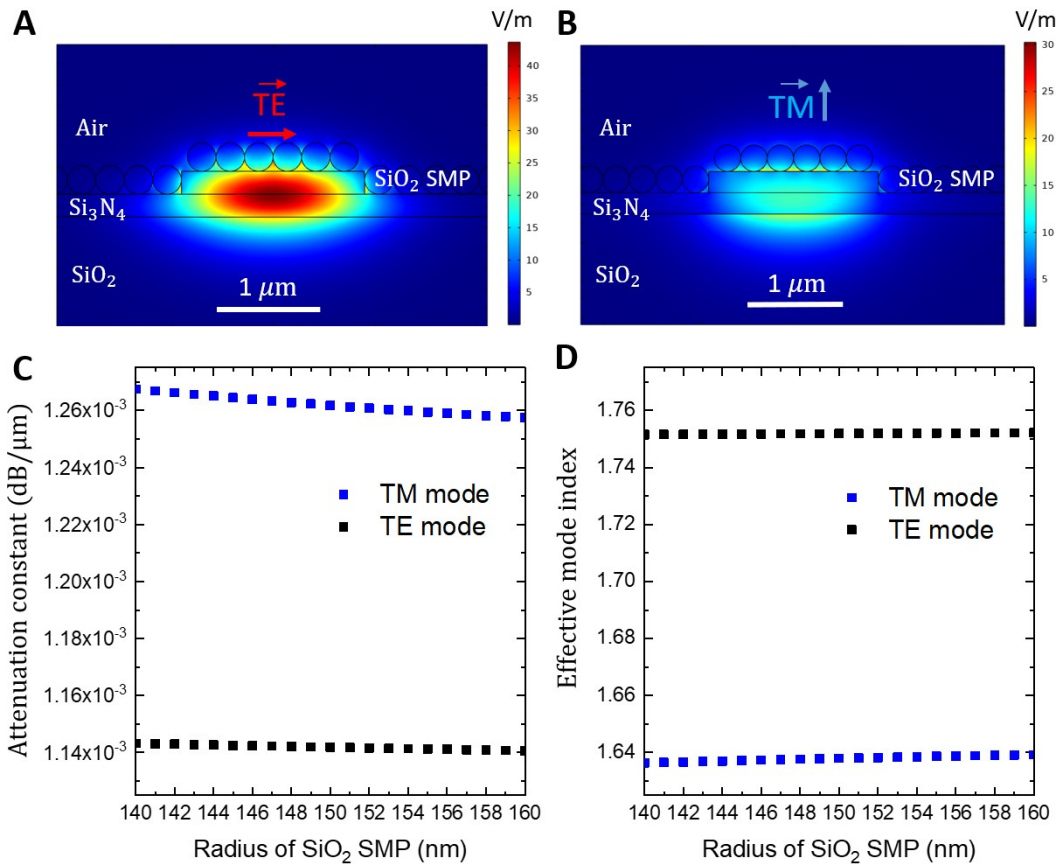
127

132 Besides uniform the diameter control of the SiO_2 SMPs, an optimal concentration was found to ensure a close-packed monolayer
133 without causing agglomeration or multilayer formation (**Fig. S7-S10**). High concentration can lead to overlapping of particles,
134 while low concentration might result in a defective monolayer with low coverage monolayer, both of which can degrade the
135 sensing performance. A uniform and well-packed monolayer ensures consistent micro-ring resonances across the sensor,
136 enhancing the overall sensitivity and reliability. Variations in particle concentration during the assembly process can lead to
137 defects and non-uniformity in the monolayer, adversely affecting the Q factor and sensitivity.

138

139 **S7   GAS SENSING PERFORMANCE BY SILICA PARTICLES COATED MICRO-RING RESONATORS**

140 To estimate the influence of CPCs on the optical characteristics of silicon nitride MRRs, and the gas sensing performance, the
141 following tasks were carried out: (1) monitoring the effect of CPC on MRR characteristics; (2) determining the relative shift of the
142 resonance position of MRRs due to introduction of saturated vapours of the studied analytes in the channel. All experimental
143 work, such as film deposition and measurements were carried out at room temperature. For the first experiment, one of the
144 channels was chosen for coating and the other channel was left as a reference with uncoated MRRs for the next step. The optimal
145 channel geometry and flow rates were determined from the previous experiments with PEI-modified micro-channels on Si_3N_4
146 surface. In the second step, vapours were pumped through the channel by using a peristaltic pump, and transmission spectral
147 characteristics were measured.
148
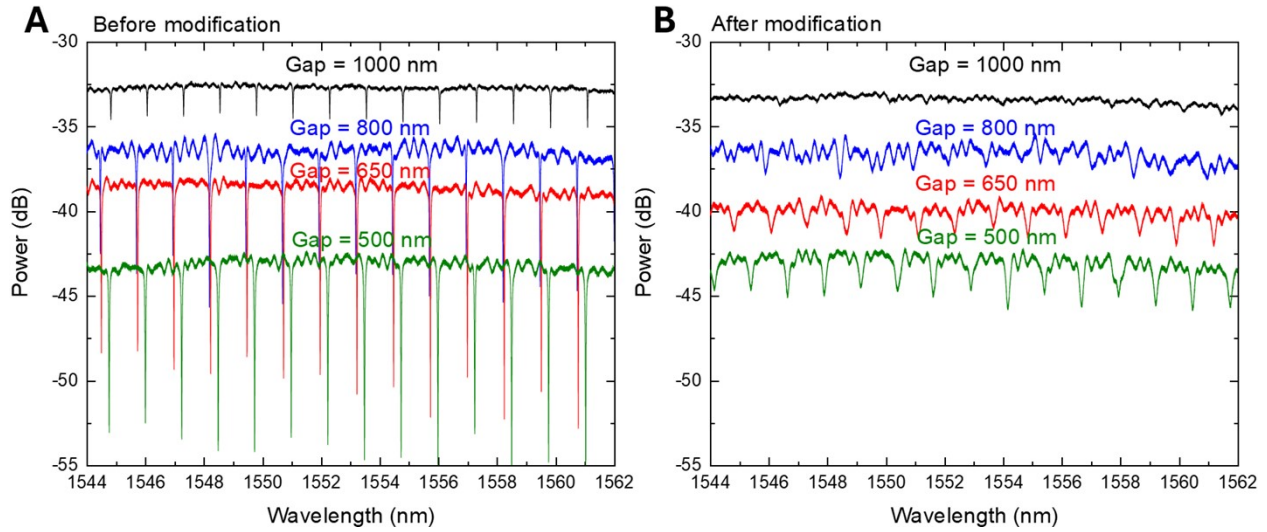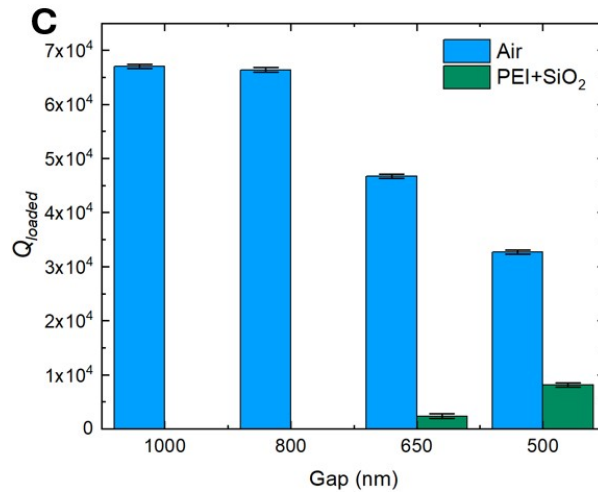
**Fig. S12. Optical characteristics of micro-ring resonators uncoated/coated by silica particles.** The comparison between the transmitted spectra of MRR1, MRR2, MRR3, and MRR4 before (**A**) and after depositing PEI+SiO$_2$ cladding (**B**), correspondingly. There are four devices: MRR1 (gap = 1000 nm; $y_{shift} = 0\ dB$), MRR2 (gap = 800 nm; $y_{shift} = 10\ dB$), MRR3 (gap = 650 nm; $y_{shift} = 5\ dB$) and MRR4 (gap = 500 nm, $y_{shift} = 1\ dB$). (**C**) Bar chart of the external quality factor of resonators before (air cladding) and after PEI+SiO2 cladding deposition of the silica film.

For optimization of MRR geometry during PEI modification, the gaps between bus and ring waveguides were 1000 nm, 800 nm, 650 nm, and 500 nm for respective resonators going from left to right in both rows. The MRR on the far left of **Fig. S10** is labeled as MRR1, and consequently, the devices going from left to right are labeled as MRR2 to MRR 4. The left end of the micro-channels was used as the inlet, and the opposite end was used as the outlet. As it was demonstrated in the recent works,[s6-s8] the chip was kept constant during the experiment. The microfluidic-nanophotonic sensor was placed upon an adjustable 3D stage with a heater and thermometer. The proportional-integral-derivative PID controller was used for stabilizing the temperature on the table to be equal to 25°C. To provide TE single-mode propagation regime, focusing grating couplers with an efficiency of 18% to input & output optical radiation from the photonic chip were used.[s9] The polarization controller was used to achieve maximum signal at transmission, which corresponded to the TE - mode. **Fig. S12 A, B** demonstrates the transmission spectrum for MRRs with different gaps in case of uncoated/coated by silica particles of sensitive sensor surface. It was found that the deposition of silica particles to the sensitive surface of the device and gap area did not lead to significant changes in the transmission spectrum of the PIC structure. In contrast, the quality factor of the MRRs is sharply reduced with the deposition of silica particles, which makes it impossible to operate devices with wide gaps (**Fig. S12 C**).

169

170

171
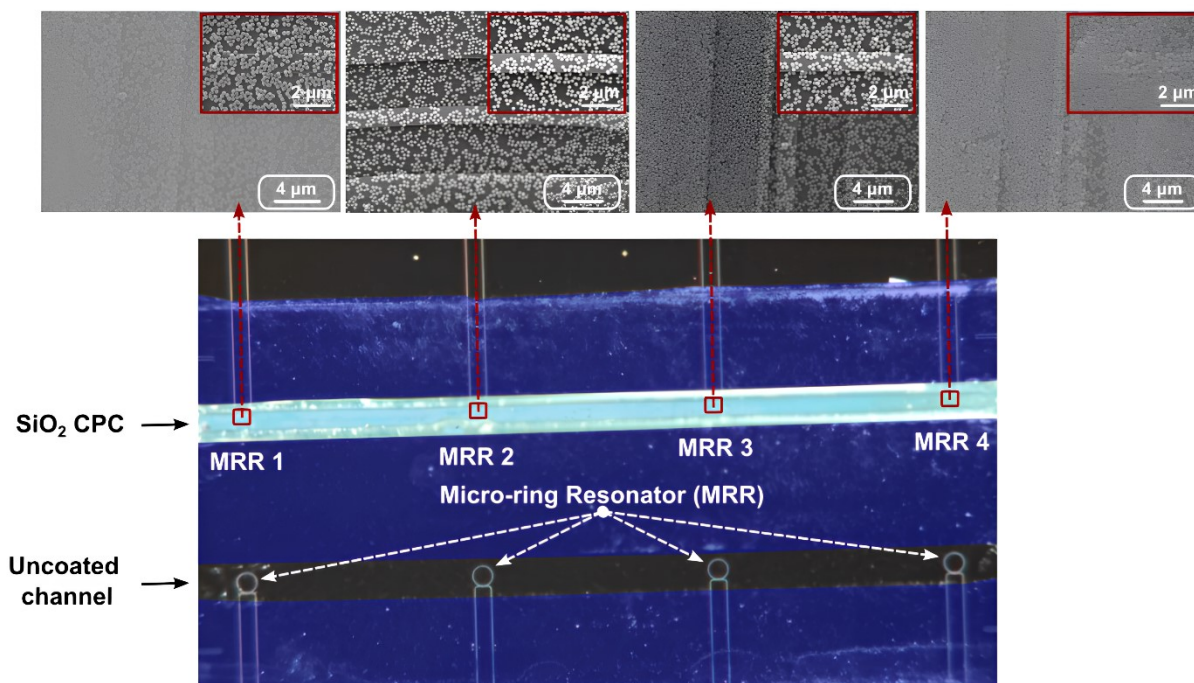
Fig. S13. The micro-ring resonators coated and uncoated by SiO₂ CPCs. (
$$v_{filling} = 5\frac{\mu L}{min}; v_{outflow} = 50\frac{\mu L}{h}; t_{stabilization} \approx 2 \; min;$$
channel parameters: 500 μm × 500 μm).

Firstly, the photonic chip with MRRs and PDMS chip were manually stacked together by using a custom holder with adjustable XYZ coordinates and angle in the XY coordinates. The microfluidic chip contained two 13 mm long, 500 μm wide, and 500 μm high micro-channels. The channels were aligned such that the centers of MRRs of both rows (see **Fig. S13**), coincided with the center of the channels. The colloidal suspension was first slowly pumped inside the channel at a flow rate of 10 μL/min and withdrawn at a flow rate of 50 μL/h. During experiments, the temperature of the copper stage was slowly increased to 60°C and left for drying for one hour. Afterward, the chip was slowly cooled down to room temperature, again heated for a few minutes at 60°C after depositing coating in one of the channels.

The formation of the *hcp* silica layer on the surface might be an extremely complex process even on a planar substrate surface. Particularly, the principles of dense layer formation are in conjunction of the DLVO theory, the Derjaguin-Muller-Toporov adhesion theory, the Johnson-Kendal-Roberts theory, and the stability of laminar flow in the micro-channels. Therefore, taking into account the aspects of these theoretical models and the complicated structure of the nano-patterned surface of the micro-ring resonators and waveguides, we would like to note some significant parameters, which might affect the lattice structure of silica CPC on the micro-ring resonators.

First, the preliminary modification of the Si_3N_4 surface by PEI for the surface of the channels creates additional contacts between individual particles and the walls of nano-patterned cavities, particularly by electrostatic interaction between them and due to the artificial surface roughness of the nano-patterned surface (see **Fig. S5**). Additionally, we may estimate the ratio θ between the number of silica particles in the suspension and the maximum number of surface sites for *hcp* formation of CPC. As the depth of the nano-pattern is 225 ± 12 nm which is less than the diameter of an individual particle (d = 300 nm), we may conclude that the walls of the nano-patterned cavities do not provide the additional sites for adhesion of the particles. Considering the dimensions $l \times w \times h$ of the microfluidic channel equal to 10 × 0.5 × 0.5 mm, we calculate the ratio between the number of silica particles in the suspension N_{SiO2} and the number of active sites N_{sites} according to *Equations 2 – 4*:

$$N_{SiO2} = \frac{C_{SiO2} \cdot l \cdot w \cdot h}{\frac{4}{3}\pi \cdot R^3 \cdot \rho_{SiO2}}$$

(2)

$$N_{sites} = \frac{\varphi \cdot l \cdot w}{\pi \cdot R^2}$$

(3)

$$\theta = \frac{N_{SiO2}}{N_{sites}} \approx 1.6 \cdot 10^3$$

,

(4)

where $l \cdot w \cdot h$ - dimensions of the micro-channel; c_{SiO2} – concentration of the silica particles in the ethanol suspension; $R = 150\ nm$ – radius of an individual particle; $\rho_{SiO2} \approx 2\ ^g/_{cm^3}$ – density of amorphous silica; $\varphi \approx 90.7\%$ – maximum coefficient of the surface coverage for *hcp* lattice. Thus, in these conditions, the number of silica particles is 1000 times more than the surface sites. This estimation demonstrates that such an excess concentration of silica particles might be sufficient for forming the *hcp* lattice structure of CPC.
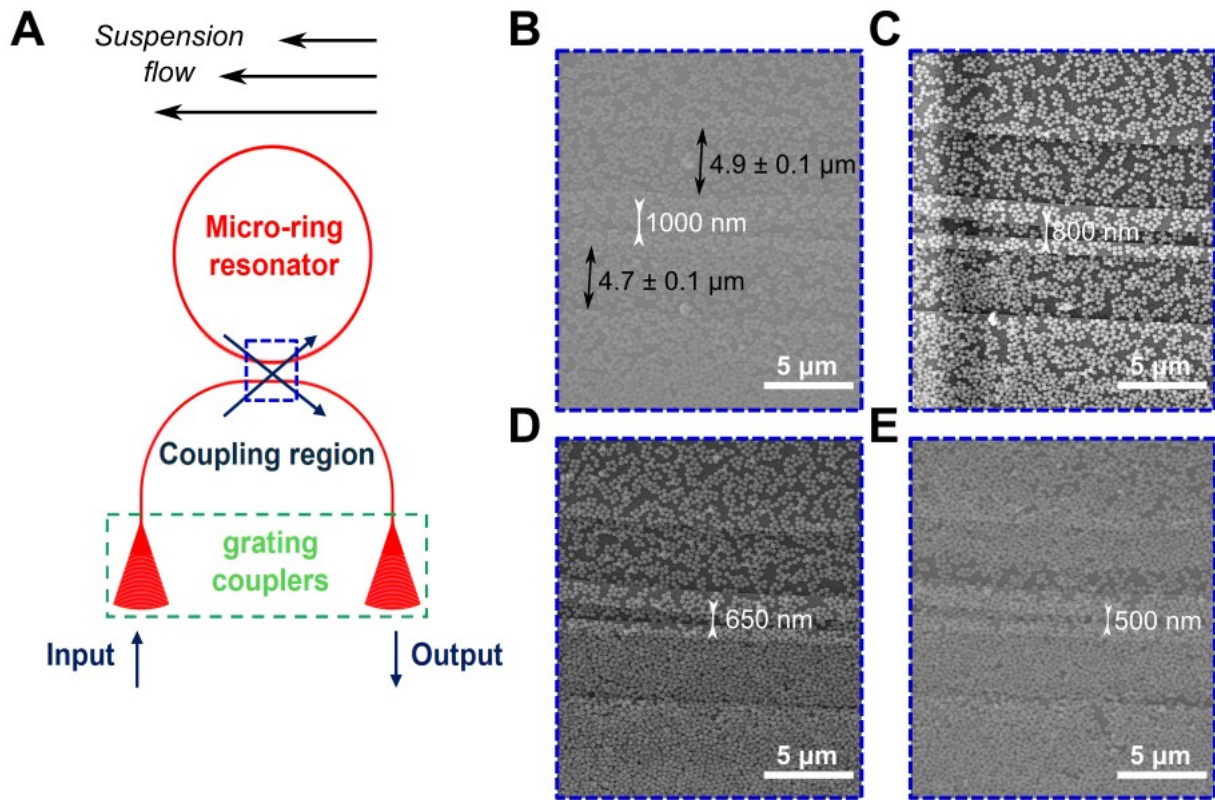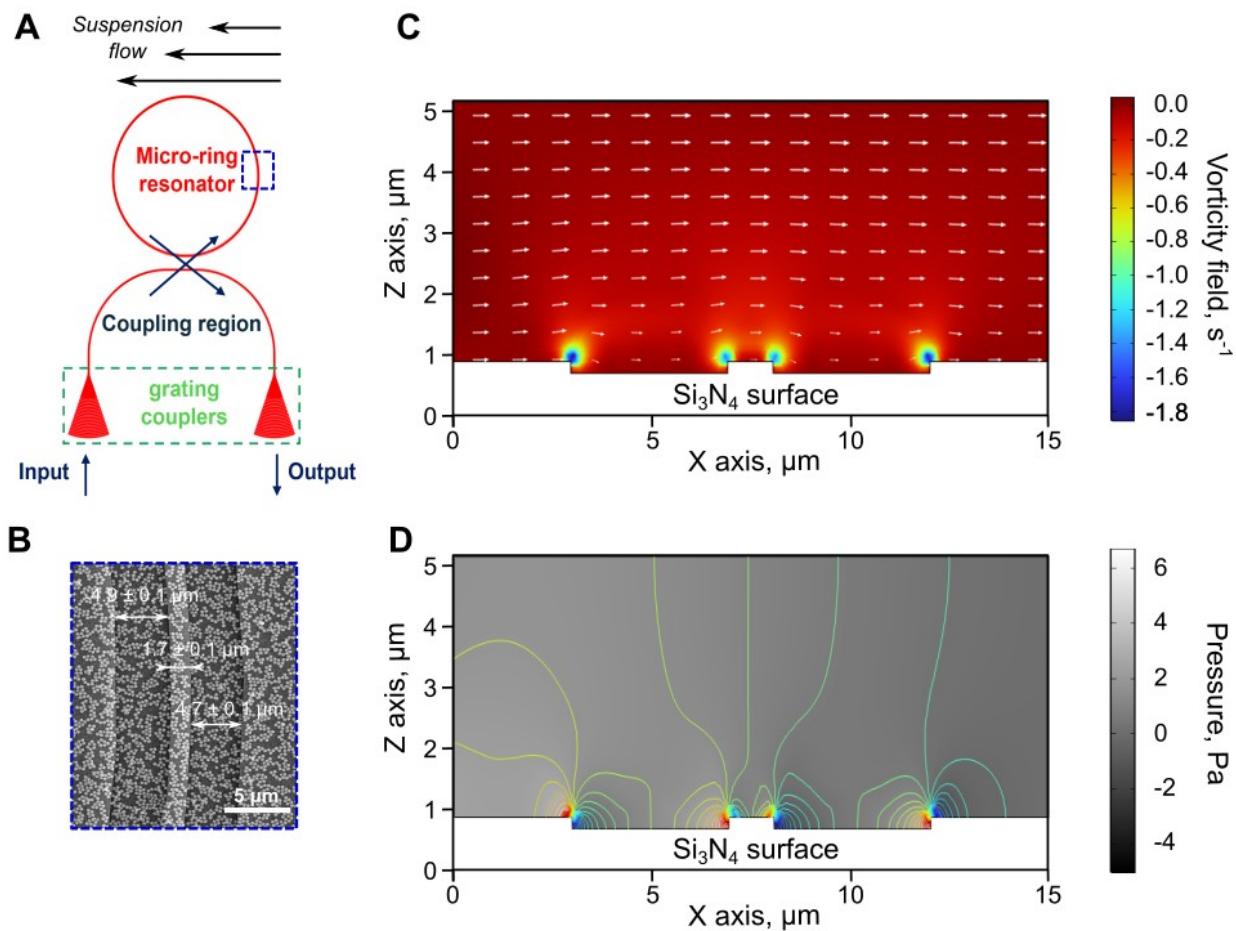

Fig. S14. The micro-ring resonator configuration (**A**) and silica layers deposited on the micro-ring resonator surfaces with a gap of 1000 nm (**B**), 800 nm (**C**), 650 nm (**D**), and 500 nm (**E**).

208 Furthermore, the structure of micro-ring resonators is quite complex for the estimation of regularities for forming *hcp* layers and
209 depends on the point, where we want to estimate the CPC formation. Here, we assessed how the CPC structure differs at the
210 contact area between the bus waveguide and MRR (**Fig. S14 A**) and the perpendicular area of the MRR towards the suspension
211 flow (**Fig. S15 A**). Analyzing the first configuration of nano-patterns and suspension flow, we observed that the CPC structure
212 inside the micro-ring and bus waveguide cavities is similar to the CPCs on the planar areas of the Si_3N_4 surface. This fact might be
213 explained due to the parallel position of the cavity lines towards the particle flow, i.e., the dislocations in the CPC structure may
214 be defined by the narrowest cavities such as the gaps between the MRR and bus waveguides (**Fig. S14 B-E**). If the width of the
215 gap is less than the doubled diameter of the particle ($< 600\ nm$), then silica particles can not be placed in the closely packed
216 structure and this provokes the formation of multilayers in the gap cavities.

217 Considering the configuration of the perpendicular orientation of the MRR cavities towards the flow (**Fig. S15 B**), we suggest that
218 in this case, the turbulent flows might appear close to the surface. Such deflection of flow state from the laminar regime to a
219 turbulent one can provide stochastic changes in the direction and velocity of the particles in the channel. We constructed the
220 COMSOL model of the flow distribution of pure ethanol in the studied microfluidic channel and surface patterns (**Fig. S15 C, D**),
221 and assessed the possibility of the appearance of the additional vorticity fields near the Si_3N_4 surface. Wherein, we assumed the
222 laminar regime of the flow at the input of the channel ($Reynolds\ number, Re = 500$). The additional vorticity fields as well
223 as the fluid pressure increase were observed at the borders of the nano-patterned cavities. Thus, we confirmed the formation of
224 turbulent flows, which might improve the structure of the CPC lattice inside the cavities, although to make the dislocations for
225 the CPC structure on the total chip surface due to the random behaviour of particle flows.
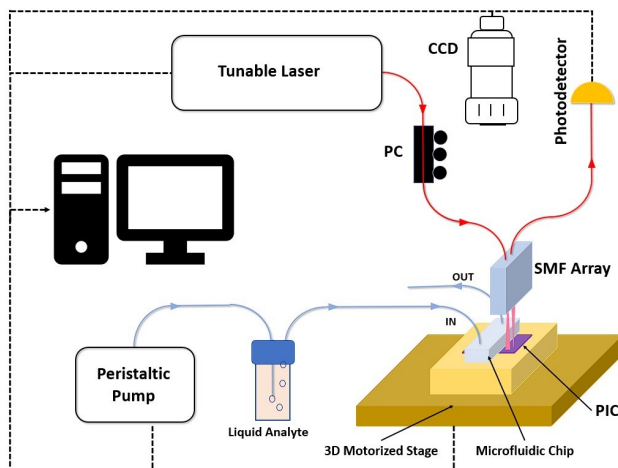

226

227 **Fig. S15.** The micro-ring resonator configuration (**A**) and silica layers deposited on the micro-ring resonator surface (**B**).
228 Distribution of vorticity flow field (**C**) and fluid pressure (**D**) for the ethanol flow in the microfluidic channels modeling by COMSOL
229 Multiphysics ($Reynolds\ number, Re = 500$).

230

231

232

Fig. S16. Experimental setup for gas sensing performance with silica monolayers modified O-ring resonators. The dashed black lines indicate electronic connections, blue lines-microfluidic, and orange lines optical fiber connections.

To understand the effects of PEI modification and convective assembly, first, the transmission spectrum of all four devices was measured when there was only DI water in the channels. Following DI water, measurements were carried out before as well as after 20 minutes of pumping 1 mg/ml solution of PEI in DI water. Furthermore, the channel was washed by pumping DI water for 10 minutes. All reagents were pumped at a flow rate of 20 μL/min, except the colloidal silica suspension. Similarly, the transmission spectra were measured after convective assembly of particles and drying for one hour.

In the second part of the experiment, the setup consisted of main elements presented in **Fig. S16**. Mainly, three types of analyte vapours were used, i.e., DI water, ethanol, and acetone. A peristaltic pump and Drexel flask containing the studied analyte were connected in series with the inlet of the microfluidic setup. The air from the surroundings was pumped inside the liquid analyte to form air bubbles that quickly become saturated with the analyte molecules, compared to conventional vapours evaporated from a bulk surface. Another tube connected the microfluidic channels with the Drexel flask, and the saturated vapours were pumped towards the sensing elements.

246
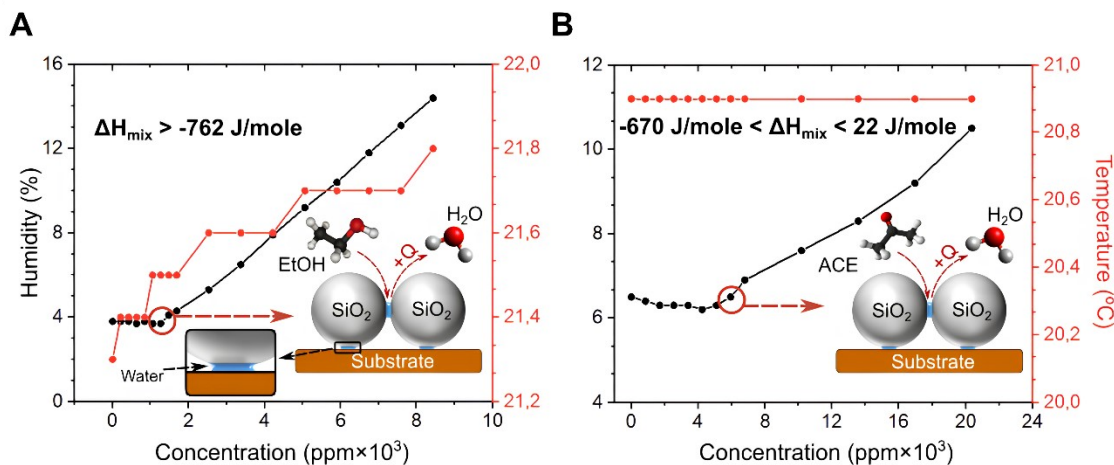
Fig. S17. Influence of concentration of VOCs on the humidity and temperature by testing ethanol (A) and acetone (B) vapours.

Initially, measurements without air flow in the channels were performed and used as a reference point. Following that, the transmission spectrum of MRR was measured after five minutes of pumping water vapours at the flow rate of 20 μL/min. Before proceeding to the next analyte, the room air inside the channel was pumped at 100 μL/min to observe the effects of air flow on

251 capillary condensation of analytes. Similarly, the vapours of ethanol and acetone were introduced respectively after five minutes
252 of air flow to determine their effects on condensed analytes.

253 **S8   ADVANTAGE OF THE PROPOSED CONCEPT**

254 Many methods for breath analysis have been explored throughout the last decade, from the earliest methods, as for instance,
255 gas chromatography coupled with mass spectrometers,[s10] to the most recent ones, such as electronic noses (E-noses).[s11] However,
256 the limitations of mass spectrometry include its inability to differentiate between two volatile compounds that share the same
257 most pronounced mass-to-charge ratio, potentially leading to ambiguities in compound identification. In turn, despite the
258 advantages of E-noses related to high sensitivity and cost-effectiveness, E-noses suffer from several significant drawbacks, e.g., a
259 need for a training prior to the use and proper calibration to cope with the discreteness.[s12] Other than conventional methods,
260 optical spectroscopic methods using lasers have also been the center of attention.[s13] Despite that, such techniques are not
261 portable, rather complex and expensive. PIC-based sensors majorly operate based on the refractive index changes in a surface
262 layer of waveguides. This is a method similar to laser spectroscopic techniques, information of gases can be gathered based on
263 the absorption occurring in an optical mode of the waveguide. Although, the main challenge is to reach lower limits of detection.
264 To overcome this challenge, modification of the surface of the photonic circuits is commonly applied. Mostly, chemically
265 functionalized nano-porous materials,[s14] analyte-sensitive organic material,[s15] or metal-organic framework coatings[s16] are
266 preferred. The activity in these areas indicates that with chemically functionalized porous coatings and their combination with
267 the PICs, gas sensors for biomedical applications can be fully realized. However, this still poses similar issues to that of chemical
268 semiconductor sensors. The performance of chemisorption-based sensing elements always deteriorates over time.
269
270 **Table S1.** Colloidal Photonic Crystals (CPCs) for gas sensing applications

Sensor signal generation	Sensing material	CPC formation method	Detected analytes	Reference
Whispering gallery mode	Mesoporous SiO_2 microspheres decorated by Pd nanoparticles	Dip-coating	Hydrogen	[s16]
Bragg stacks	Mesoporous SiO_2 nanoparticles and TiO_2 sols	Spin-coating	Toluene	[s17]
Resistivity / Reflectance	PEDOT/PPy inverse opals	Electrodeposition	Ammonia	[s18]
Bragg stacks	Alternating SiO_2 / TiO_2 nanoparticle layers functionalized with different alkoxysilanes	Spin-coating	Alcohols / Volatiles from bacteria species	[s19]
Bragg stacks	SiO_2 monolayer on Ta_2O_5/SiO_2 photonic crystal surface	Dip-coating	Acetone, Ammonia, Ethanol, 2-Propanol	[s5]
Transmittance / Bragg peak wavelength shift	Polystyrene nanoparticle monolayer	Dip-coating	Ethanol	[s20]
Bragg stacks	Alternating layers of amorphous poly(p-	Spin-coating	Carbon tetrachloride, benzene, 1,2-	[s21]

phenylene oxide) and cellulose acetate	dichlorobenzene

271

272 The developed sensor based on a combination of PICs and microfluidics has the potential to bring new opportunities in gas

273 sensing, and various other sectors including colloidal science, thin film coatings on inert surfaces, gas sensing, colloidal photonic

274 crystals for photonic integrated circuits with new functionalities, the study of optical properties of bound water in nanopores.

275 Microfluidic convective assembly helps to achieve the specific patterns of silica CPCs on Si_3N_4 substrates with a surface coverage

276 coefficient of up to 59%. In addition, the integration of CPC with PIC on Si_3N_4 platform enhances the optical PIC sensing

277 capabilities in terms of sensitivity and specificity due to leveraging the unique properties of CPCs, coupled with the high optical

278 transparency of Si_3N_4 in the near IR range.

279

280 In terms of real-time operation, this sensor will handle each analyte differently depending on changes in the effective refractive

281 index of the surface layer. **Fig. S18** shows the dependence of the relative shift of resonance positions in the transmission spectrum

282 of MRRs recorded by introducing DI water, ethanol, and acetone vapours. Relying on the average change in the relative resonance

283 position shift over time and on the experimental noise of the setup equal to about 1 pm is demonstrated in our previously study,[s7,]

284 [s8] the average response time of the system for ethanol vapours is ≈ 7 s, for acetone vapours ≈ 18 s, respectively. Compared to

285 other sensor systems for real-time ethanol vapour detection, the current configuration shows promising results when compared

286 to commercially available electrochemical (< 30 s),[s23] semiconductors (60 - 90 s)[s24] and optical sensors (6 s)[s25] for exhaled breath

287 analysis on the alcohol intoxication degree. Still, the evaluation of the determination range and the number of cycles of continuous

288 operation of the proposed sensor requires extra studies.

289

290 Additionally, we estimated the analytical characteristics of the proposed sensor. Here, the micro-ring with the deposited silica

291 layer is exposed to the saturated vapours of acetone and ethanol. To estimate the pressure of the saturated vapours in the micro-

292 channels we used the Antoine equation.[s26] Applying the assumption of the ideal gas, the sensitivity coefficients were equal to -

293 $5.9 \cdot 10^{-4}$ pm/ppm and $-5.7 \cdot 10^{-5}$ pm/ppm for ethanol and acetone vapours, respectively. That means such sensing configuration is

294 ~10 times sensitive to ethanol vapours than to acetone ones. This is supported by the values of LoD for ethanol and acetone which

295 are equal to $5.1 \cdot 10^3$ ppm and $53 \cdot 10^3$ ppm, accordingly.
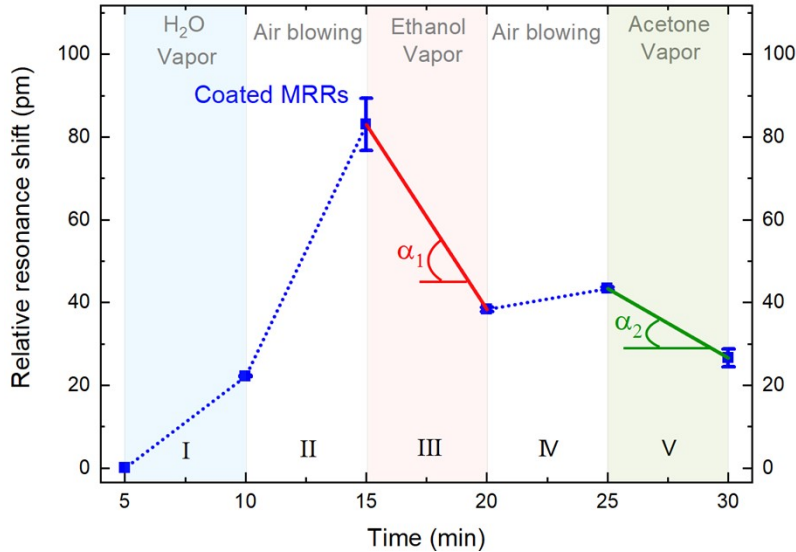
296

297 **Fig. S18. Gas sensing performance for micro-ring resonators coated and uncoated by SiO₂ film:** Relative shift of resonance

298 positions in the transmission spectrum of modified MRR recorded by introducing DI water, ethanol, and acetone vapours. The

299 blue dashed line showed the shifting of the resonance position of the ring waveguides coated by SiO₂ monolayers. The red and

300 green solid lines showed the shifting of the resonance position of the ring waveguides coated by SiO₂ monolayers for ethanol and

301 acetone vapours, respectively. α_1 (-8.93 pm/min) and α_2 (-3.35 pm/min) are the derivatives of the resonance shift over time for

302 the modified sensor for the ethanol and acetone vapours, respectively. Error bars coloured blue solid line are the standard

303 deviation of coated MRRs.

REFERENCES

s1   Open Source Computer Vision, https://docs.opencv.org/4.x/d7/d4d/tutorial_py_thresholding.html, (accessed 7 February 2024).

s2   D. Feng, D. Weng and J. Wang, *Micromachines*, 2018, **9**.

s3   T. Ohmi, *J. Electrochem. Soc.*, 1996, **143**, 2957–2964.

s4   T. Yamashita and K. Ando, *Ultrason. Sonochem.*, 2019, **52**, 268–279.

s5   V. Zaytsev, T. I. Ermatov, F. S. Fedorov, N. Balabin, P. O. Kapralov, J. V. Bondareva, D. O. Ignatyeva, B. N. Khlebtsov, S. S. Kosolobov, V. I. Belotelov et al., *Analytical chemistry*, 2022, **94**, 12305–12313.

s6   A. Kuzin, V. Chernyshev, V. Kovalyuk, P. An, A. Golikov, S. Svyatodukh, S. Perevoschikov, I. Florya, A. Schulga, S. Deyev et al., *Applied Physics Letters*, 2023, **123**.

s7   A. Kuzin, K. Panda, V. Chernyshev, I. Florya, V. Kovalyuk, P. An, A. Golikov, G. Chulkova, D. Kolesov, D. Gorin et al., *Applied Physics Letters*, 2024, **124**.

s8   A. Kuzin, V. Chernyshev, V. Kovalyuk, P. An, A. Golikov, R. Ozhegov, D. Gorin, N. Gippius and G. Goltsman, *Optics Letters*, 2022, **47**, 2358–2361.

s9   A. Kuzin, V. Kovalyuk, A. Golikov, A. Prokhodtsov, A. Marakhin, S. Ferrari, W. Pernice, N. Gippius and G. Goltsman, *Journal of Physics: Conference Series*, 2019, p. 012181.

s10   U. Tisch, I. Schlesinger, R. Ionescu, M. Nassar, N. Axelrod, D. Robertman, Y. Tessler, F. Azar, A. Marmur, J. Aharon-Peretz et al., *Nanomedicine*, 2013, **8**, 43–56.

s11   V. H. Tran, H. P. Chan, M. Thurston, P. Jackson, C. Lewis, D. Yates, G. Bell and P. S. Thomas, *IEEE Sensors Journal*, 2010, **10**, 1514–1518.

s12   F. S. Fedorov, N. P. Simonenko, P. V. Arsenov, V. Zaytsev, T. L. Simonenko, B. V. Goikhman, I. A. Volkov, E. P. Simonenko and A. G. Nasibulin, *Applied Surface Science*, 2022, **606**, 154717.

s13   R. Claps, F. V. Englich, D. P. Leleux, D. Richter, F. K. Tittel and R. F. Curl, Applied Optics, 2001, **40**, 4387–4394.

s14   G. Antonacci, J. Goyvaerts, H. Zhao, B. Baumgartner, B. Lendl and R. Baets, *APL photonics*, 2020, **5**.

s15   R. Janeiro, R. Flores and J. Viegas, Scientific reports, 2019, **9**, 17099.

s16   J. Tao, X. Wang, T. Sun, H. Cai, Y. Wang, T. Lin, D. Fu, L. L. Y. Ting, Y. Gu and D. Zhao, *Scientific reports*, 2017, **7**, 41640.

s17   Y. Yue, H. Ding and C. Chen, *International Journal of Hydrogen Energy*, 2021, **46**, 1403–1410.

s18   J. Kobler, B. V. Lotsch, G. A. Ozin and T. Bein, *ACS nano*, 2009, **3**, 1669–1676.

s19   Q. Zhong, H. Xu, H. Ding, L. Bai, Z. Mu, Z. Xie, Y. Zhao and Z. Gu, *Colloids and Surfaces A: Physicochemical and Engineering Aspects*, 2013, **433**, 59–63.

s20   L. D. Bonifacio, D. P. Puzzo, S. Breslav, B. M. Willey, A. McGeer and G. A. Ozin, *Advanced Materials*, 2010, **22**.

s21   R. Pernice, G. Adamo, S. Stivala, A. Parisi, A. C. Busacca, D. Spigolon, M. A. Sabatino, L. D'Acquisto and C. Dispenza, *Optical Materials Express*, 2013, **3**, 1820–1833.

s22   P. Lova, C. Bastianini, P. Giusto, M. Patrini, P. Rizzo, G. Guerra, M. Iodice, C. Soci and D. Comoretto, *ACS applied materials & interfaces*, 2016, **8**, 31941–31950.

s23   Dräger UK, https://www.draeger.com/en_uk/Products/Alcotest-6000 (accessed June 25, 2024).

s24   Alco Prevention Canada, https://alcoprevention.com/en/product/alco-mini-08-breathalyzer/ (accessed June 25, 2024)

s25   Laser Systems, https://www.lsystems.ru/en/product/alcoframes/ (accessed June 25, 2024)

s26   A. F. N. W. Adi, T. G. Wulanndari, A. Wiguno and K. Kuswandi, *IOP Conf. Ser.: Mater. Sci. Eng.,* 2021, **1053**, 012137.